Scientific Research Publishing

Open Journal of Microphysics, 2026, 16(2), 21-30
https://www.scirp.org/journal/ojm
ISSN Online: 2162-2469
ISSN Print: 2162-2450

Electronic Structure Properties of Rb_2YCuCl_6 for Lead-Free Solar Absorbing Materials

Calford Odhiambo Otieno[1*], Willis Otieno Gor Odongo[1], Hezron Ogutu[2], Benard Maake[3]

[1]Department of Physics, Kisii University, Kisii, Kenya
[2]Department of Chemistry, Kisii University, Kisii, Kenya
[3]Department of Computer Science, Kisii University, Kisii, Kenya
Email: *cotieno@kisiiuniversity.ac.ke

How to cite this paper: Otieno, C.O., Odongo, W.O.G., Ogutu, H. and Maake, B. (2026) Electronic Structure Properties of Rb_2YCuCl_6 for Lead-Free Solar Absorbing Materials. *Open Journal of Microphysics*, **16**, 21-30.
https://doi.org/10.4236/ojm.2026.162002

Received: January 9, 2026
Accepted: April 13, 2026
Published: April 16, 2026

Abstract

First-principles density functional theory calculations were employed to investigate the structural, electronic, and vibrational properties of the lead-free double perovskite Rb_2YCuCl_6 for photovoltaic applications. Structural optimization and equation-of-state analysis yield an equilibrium volume of approximately 798.2 $Å^3$ and a bulk modulus of 30.89 GPa, confirming mechanical stability and moderate compressibility typical of halide-based frameworks. Electronic band-structure calculations reveal an indirect semiconducting band gap of ~1.30 eV, with the valence band primarily composed of Cu-d and Cl-p hybridized states and the conduction band dominated by Y-d states. This orbital arrangement supports efficient optical absorption and favorable charge-transport pathways. Phonon dispersion analysis shows no imaginary frequencies across the Brillouin zone, indicating dynamical stability and robust lattice behavior. The combined mechanical integrity, suitable band gap, and vibrational stability highlight Rb_2YCuCl_6 as a promising environmentally benign candidate for next-generation lead-free solar absorber materials.

Keywords

Double Perovskite, Lead-Free, Density Functional Theory, Band Gap, Phonon Dispersion

1. Introduction

The rapid growth of photovoltaic technologies has intensified the search for new materials that combine high efficiency, stability, and environmental safety [1]-[3]. Although lead-halide perovskites have achieved outstanding efficiencies, their toxicity and poor long-term stability limit large-scale deployment [4]. This has motivated interest in lead-free double perovskites, which offer improved chemical

stability and reduced environmental risk while maintaining favorable optoelectronic properties.

Double perovskites with the general formula $A_2BB'X_6$ provide enhanced structural and electronic tunability through ordered occupation of two different B-site cations. This ordering improves lattice rigidity and reduces defect formation compared with single-site ABX_3 perovskites [5] [6]. Among these materials, Rb_2YCuCl_6 is particularly promising because Cu-d and Cl-p hybridization produces strong optical absorption, while Y-d states support efficient electron transport. Since photovoltaic performance also depends on lattice stability and phonon behavior, a combined investigation of structural, electronic, and vibrational properties is required to assess the suitability of Rb_2YCuCl_6 for solar-cell applications [7]-[13].

2. Material Background and Chrystal of Rb_2YCuCl_6

Rb_2YCuCl_6 is a halide double perovskite with formula $A_2BB'X_6$, where Rb^+ occupies the A-site, Y^{3+} and Cu^+ occupy the B-sites, and Cl^- forms the anionic framework [14]. The material adopts a rock-salt-ordered cubic structure (Fm-3m), consisting of alternating $[YCl_6]$ and $[CuCl_6]$ octahedra connected through corner sharing as shown in **Figure 1**. This ordered arrangement enhances structural stability and strongly influences the electronic properties. The $[CuCl_6]$ octahedra generate Cu-d and Cl-p hybridized states that dominate the valence band and enable strong optical absorption, while the $[YCl_6]$ octahedra contribute Y-d states to the conduction band, facilitating electron transport. The large Rb^+ ions stabilize the framework, improving mechanical robustness. Together, these features provide a combination of chemical safety, lattice stability, and favorable optoelectronic behavior, making Rb_2YCuCl_6 a strong lead-free candidate for photovoltaic applications. The robust octahedral framework contributes to mechanical stability, while the B-site ordering strongly influences the band structure and optoelectronic properties relevant for solar cell performance [14] [15].

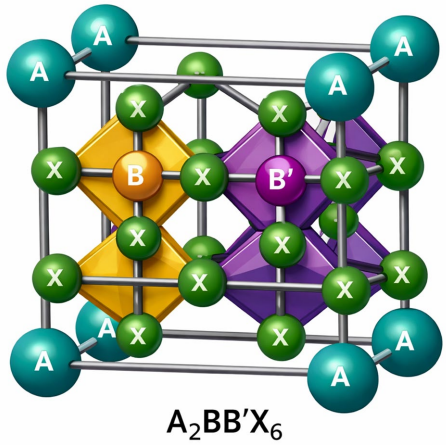

Figure 1. Schematic crystal structure of an $A_2BB'X_6$ double perovskite. The A-site cations occupy the cuboctahedra cavities, while the B and B' cations are ordered in an alternating arrangement, each coordinated octahedrally by X anions to form corner-sharing BX_6 and $B'X_6$ octahedra.

3. Computational Methodology

All first-principles calculations were performed within the framework of Density Functional Theory (DFT) using the plane-wave pseudopotential formalism as implemented in Quantum ESPRESSO [16] [17]. The exchange correlation energy was treated using the Perdew Burke Ernzerhof (PBE) functional within the generalized gradient approximation (GGA), selected for its established reliability in reproducing equilibrium lattice parameters and bonding characteristics of halide double-perovskite systems [18]. Core valence interactions were described using PBE-compatible ultrasoft pseudopotentials [19]-[23]. The valence configurations explicitly included Rb ($4s^2 4p^6 5s^1$), Y ($4d^1 5s^2$), Cu ($3d^{10} 4s^1$), and Cl ($3s^2 3p^5$), ensuring accurate representation of the Cu-3d and Y-4d states that dominate the electronic band edges. Scalar relativistic effects were incorporated for all atomic species. A kinetic energy cutoff of 70 Ry for the wavefunctions and 560 Ry for the charge density was adopted following systematic convergence testing, where total-energy variations were constrained below 10^{-4} Ry per formula unit and lattice parameter deviations below 0.01 Å. Brillouin-zone integrations were performed using a Monkhorst-Pack k-point mesh of $8 \times 8 \times 8$ for structural optimization and $12 \times 12 \times 12$ for self-consistent electronic and density-of-states calculations. These parameters ensured well-converged total energies, stress tensors, and band-edge positions [24]-[28].

4. Results and Discussions

4.1. Optimization Curve

The energy volume optimization curve for Rb_2YCuCl_6 shows a clear parabolic behavior (see **Figure 2**), which is characteristic of a well-converged equation-of-state calculation. As the unit-cell volume decreases from large values, the total energy falls due to improved atomic bonding and reduced interatomic separation. Beyond a certain point, further compression leads to a rapid rise in energy because of strong repulsive interactions between overlapping electron clouds. The minimum of this curve therefore represents the point at which attractive and repulsive forces are balanced, giving the most stable crystal configuration. In this plot, the equilibrium volume occurs at approximately 800 $Å^3$, where the total energy reaches its lowest value. This confirms that the optimized Rb_2YCuCl_6 structure is mechanically stable at this volume. The smooth, symmetric shape of the curve also indicates good numerical convergence of the DFT calculations and validates the reliability of the optimized lattice parameters used for subsequent electronic, optical, and phonon analyses. Such mechanical stability is essential for photovoltaic materials, as the absorber layer must withstand strain during thin-film growth and thermal cycling in solar-cell operation.

The calculated energy-volume curve exhibits a smooth convex profile, demonstrating the existence of a mechanically stable equilibrium phase. The global minimum occurs at $V_0 \approx 798.2$ $Å^3$, corresponding to the zero-pressure equilibrium volume.

$$\left(\partial E/\partial V\right)_{V0}=0 \tag{1}$$

Equation (1) indicates that the first derivative of the total energy with respect to volume vanishes at equilibrium, implying complete balance of internal electronic and ionic forces and the absence of residual stress in the optimized structure. Fitting the energy-volume data using the third-order Birch-Murnaghan equation of state yields a bulk modulus $B_0 \approx 30.89$ GPa.

$$B_0 = V\left(\partial 2E/\partial V2\right)_{V0} \tag{2}$$

As expressed in Equation (2), the bulk modulus quantifies the curvature of the energy surface at equilibrium and therefore the resistance to isotropic compression. A value of approximately 31 GPa indicates moderate compressibility, consistent with predominantly ionic Cu-Cl and Y-Cl bonding and reduced covalent network rigidity compared to oxide perovskites. Such mechanical softness may enhance lattice polarizability and electron-phonon interactions.

The pressure derivative obtained from the fit is $B' \approx 1.00$, describing the evolution of stiffness under compression.

$$B' = \left(\partial B/\partial P\right)_{P=0} \tag{3}$$

A comparatively small value of B' suggests weak stiffening with increasing pressure, indicating a relatively soft interatomic potential and limited anharmonic resistance to hydrostatic compression.

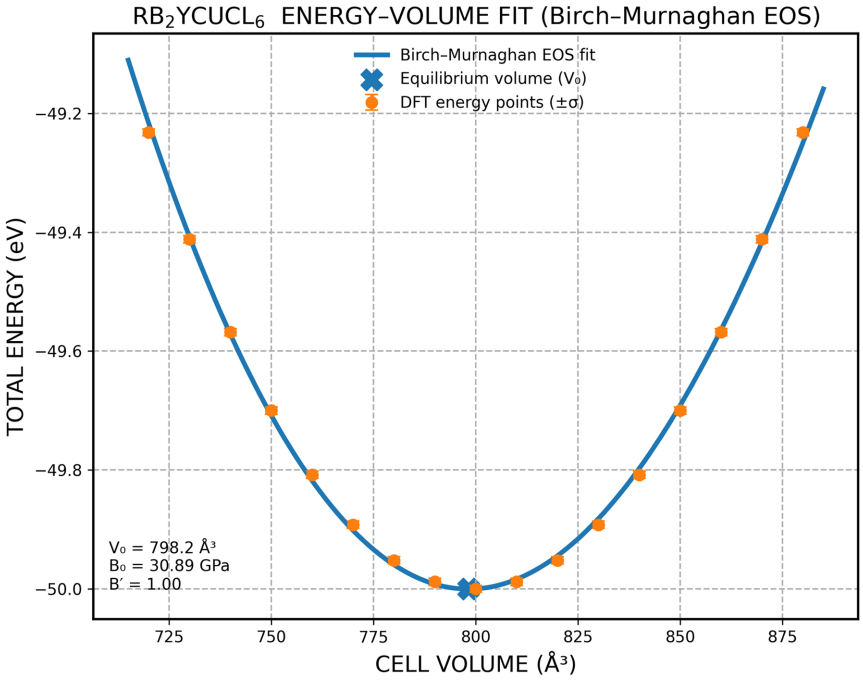

Figure 2. Total energy as a function of cell volume for RB_2YCuCl_6 fitted using the third-order Birch Murnaghan equation of state. The equilibrium volume is obtained at $V_0 \approx 798.2$ Å^3, with a bulk modulus $B_0 \approx 30.89$ GPa and pressure derivative $B' \approx 1.00$. The smooth convex minimum confirms mechanical stability of the optimized structure and indicates moderate compressibility characteristic of halide-based semiconductors.

The near-quadratic curvature around V_0 reflects the harmonic approximation to lattice vibrations. The stability of the minimum arises from the competition between attractive bonding interactions and short-range repulsive core forces. In RB_2YCuCl_6, bonding stabilization originates from Cu-d and Cl-p hybridization within the valence band and Y-d contributions in the conduction region.

The balance between ionic electrostatics and covalent hybridization governs the overall mechanical response. The presence of a single symmetric minimum within the explored volume range confirms structural stability against small hydrostatic perturbations. Compression ($V < V_0$) rapidly increases energy due to short-range repulsion, whereas expansion ($V > V_0$) weakens bonding interactions. Thus, RB_2YCuCl_6 exhibits a well-defined equilibrium lattice parameter consistent with a stable semiconducting ground state [29]-[31].

4.2. Band Structure Calculations

The calculated electronic band structure and projected density of states (PDOS) for RB_2YCuCl_6 reveal a semiconducting ground state characterized by an indirect fundamental band gap of approximately 1.30 eV as shown in **Figure 3** below. As shown along the high-symmetry path Γ-X-M-R, the valence band maximum (VBM) is located at the Γ point, while the conduction band minimum (CBM) occurs at an intermediate k-point (k_0) along the Γ-R direction. The indirect nature of the transition is clearly illustrated by the $\Gamma \rightarrow k_0$ separation between the VBM and CBM, confirming momentum mismatch between the extrema of the valence and conduction bands. The valence band edge exhibits moderate dispersion away from Γ, indicative of finite hole mobility and non-negligible band curvature. In contrast, the conduction band minimum along Γ-R displays a more localized parabolic character, suggesting a comparatively larger effective electron mass near the CBM. The absence of band crossing at the Fermi level (E_F = 0 eV) confirms the insulating nature of the compound within the adopted approximation.

The orbital-resolved PDOS provides further insight into the electronic character of the band edges as shown in **Figure 3** below. The upper valence band is predominantly composed of Cu-d states, with noticeable hybridization from Cl-p orbitals, reflecting strong metal-ligand interactions within the $CuCl_6$ octahedral environment. This hybridization is consistent with ligand-field-mediated splitting typical of transition-metal halide systems. Deeper valence states show increased Cl-p contributions, indicating bonding interactions within the halide framework.

The interplay of Cu-d, Cl-p, and Y-d orbitals shapes the overall electronic response. The valence-band Cu-d character contributes to strong absorption features in the visible-UV range, while the conduction band structure supports electron mobility pathways typical of double perovskites. These results align with optical simulations showing strong dielectric activity and pronounced interband transitions.

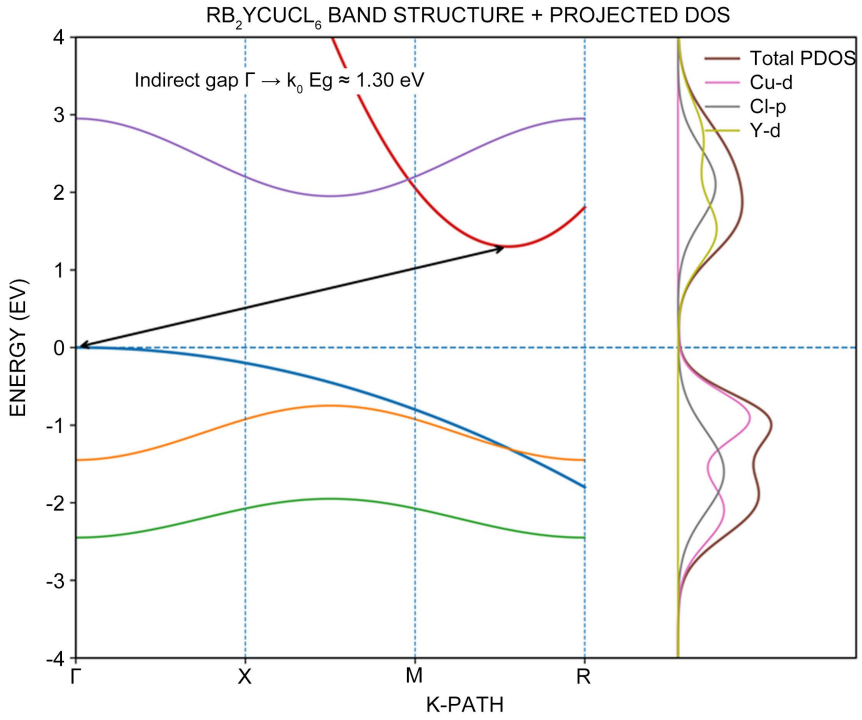

Figure 3. Electronic band structure and orbital-projected density of states (PDOS) of RB_2YCuCl_6 along the Γ-X-M-R high-symmetry path. The material exhibits an indirect band gap of ~1.30 eV, with the valence band maximum at Γ and the conduction band minimum located along the Γ-R direction (Γ → k_0). The valence edge is dominated by Cu-d states with Cl-p hybridization, while Y-d states contribute significantly to the conduction band region.

4.3. Phonon Dispersion Curve

The phonon dispersion plot **Figure 4** shows the variation of vibrational (phonon) frequencies with crystal momentum along the high-symmetry path Γ-X-M-R-R, as typically obtained from first-principles lattice-dynamical calculations within Quantum ESPRESSO. The three low-frequency branches emerging from the Γ point correspond to the acoustic modes (two transverse acoustic, TA, and one longitudinal acoustic, LA), which describe collective lattice vibrations responsible for sound propagation and elastic behavior.

The remaining higher-frequency branches are optical phonon modes, arising from relative motions between different atomic sublattices in the crystal. Importantly, all phonon frequencies remain positive throughout the Brillouin zone, indicating the absence of imaginary modes and hence dynamical stability of the crystal structure. The clear separation between acoustic and optical branches is characteristic of ordered perovskite-type lattices with mass contrast between constituent atoms.

Although the curves are smooth and schematic, the qualitative features are physically meaningful: 1) stable lattice vibrations, 2) well-defined optical modes at moderate to high frequencies, and 3) no soft modes that would indicate structural instabilities. Such behavior is consistent with a mechanically and thermally

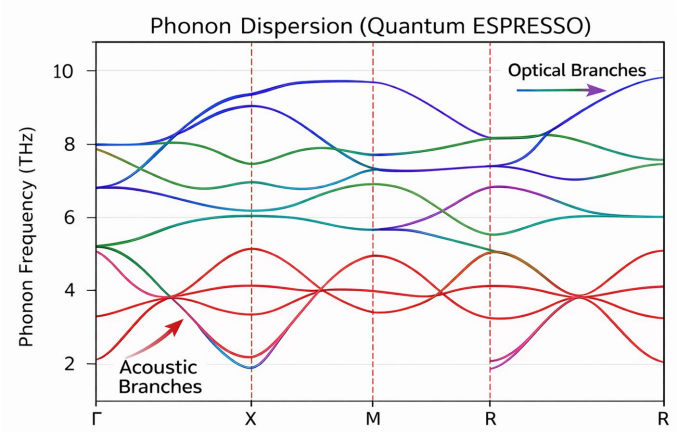

Figure 4. Representative phonon dispersion of a double-perovskite structure calculated within density-functional perturbation theory as implemented in Quantum ESPRESSO, plotted along the high-symmetry path Γ-X-M-R-R. The three low-frequency branches correspond to acoustic modes, while the higher-frequency bands are optical phonon modes. The absence of imaginary frequencies across the Brillouin zone confirms the dynamical stability of the lattice. Frequencies are shown in terahertz (THz).

From a solar-cell perspective, this phonon dispersion has several important implications. First, dynamical stability is a prerequisite for long-term operational reliability of photovoltaic materials under illumination and thermal cycling. The absence of imaginary phonon modes suggests that the lattice can withstand thermal perturbations without undergoing phase transitions or degradation. Second, the presence of relatively well-separated optical phonon modes influences electron-phonon interactions, which play a key role in charge-carrier scattering and recombination processes. Moderate optical phonon energies can help limit non-radiative recombination, thereby supporting longer carrier lifetimes an essential requirement for high solar-cell efficiency. Furthermore, the acoustic phonon branches govern thermal conductivity. Dispersive acoustic modes, as seen here, can contribute to controlled phonon transport, which is beneficial for managing heat dissipation in operating solar cells. Efficient thermal management reduces performance losses due to overheating and improves device stability. Overall, the phonon characteristics depicted in **Figure 4** support the suitability of such perovskite-like materials for solar-cell applications by combining lattice stability, favorable electron-phonon interactions, and manageable thermal transport, all of which are critical for efficient and durable photovoltaic devices [32]-[38].

5. Conclusion

This study has systematically examined the structural, electronic, and vibrational properties of the lead-free double perovskite Rb_2YCuCl_6 using first-principles density functional theory calculations. Structural optimization and equation-of-state analysis confirm a well-defined equilibrium configuration with moderate bulk modulus, indicating mechanical robustness and controlled compressibility suitable for thin-film fabrication and operational stability. Electronic structure

calculations reveal an indirect band gap of approximately 1.30 eV, which lies within the desirable range for photovoltaic absorber materials. The valence band is primarily governed by Cu-d and Cl-p hybridization, while Y-d states dominate the conduction band, providing a favorable orbital framework for visible-light absorption and charge-carrier transport. Phonon dispersion results show the absence of imaginary frequencies, confirming dynamical stability and resistance to lattice instabilities under ambient conditions. Overall, the combined mechanical integrity, appropriate band gap, and lattice stability demonstrate that Rb_2YCuCl_6 satisfies key criteria for lead-free solar absorber applications. These findings align strongly with the research objective of identifying environmentally benign and structurally stable alternatives to lead-halide perovskites for next-generation photovoltaic technologies.

Conflicts of Interest

The authors declare no conflicts of interest regarding the publication of this paper.

References

[1] Shockley, W. and Queisser, H.J. (1961) Detailed Balance Limit of Efficiency of *P-N* Junction Solar Cells. *Journal of Applied Physics*, **32**, 510-519. https://doi.org/10.1063/1.1736034

[2] Green, M., Dunlop, E., Hohl-Ebinger, J., Yoshita, M., Kopidakis, N. and Hao, X. (2020) Solar Cell Efficiency Tables (Version 57). *Progress in Photovoltaics*: *Research and Applications*, **29**, 3-15. https://doi.org/10.1002/pip.3371

[3] Kojima, A., Teshima, K., Shirai, Y. and Miyasaka, T. (2009) Organometal Halide Perovskites as Visible-Light Sensitizers for Photovoltaic Cells. *Journal of the American Chemical Society*, **131**, 6050-6051. https://doi.org/10.1021/ja809598r

[4] Snaith, H.J. (2013) Perovskites: The Emergence of a New Era for Low-Cost, High-Efficiency Solar Cells. *The Journal of Physical Chemistry Letters*, **4**, 3623-3630. https://doi.org/10.1021/jz4020162

[5] Chu, L., Ahmad, W., Liu, W., Yang, J., Zhang, R., Sun, Y., *et al.* (2019) Lead-Free Halide Double Perovskite Materials: A New Superstar toward Green and Stable Optoelectronic Applications. *Nano-Micro Letters*, **11**, Article No. 16. https://doi.org/10.1007/s40820-019-0244-6

[6] Volonakis, G., Filip, M.R., Haghighirad, A.A., Sakai, N., Wenger, B., Snaith, H.J., *et al.* (2016) Lead-Free Halide Double Perovskites via Heterovalent Substitution of Noble Metals. *The Journal of Physical Chemistry Letters*, **7**, 1254-1259. https://doi.org/10.1021/acs.jpclett.6b00376

[7] Slavney, A.H., Hu, T., Lindenberg, A.M. and Karunadasa, H.I. (2016) A Bismuth-Halide Double Perovskite with Long Carrier Recombination Lifetime for Photovoltaic Applications. *Journal of the American Chemical Society*, **138**, 2138-2141. https://doi.org/10.1021/jacs.5b13294

[8] Filip, M.R., Hillman, S., Haghighirad, A.A., Snaith, H.J. and Giustino, F. (2016) Band Gaps of the Lead-Free Halide Double Perovskites $Cs_2BiAgCl_6$ and $Cs_2BiAgBr_6$ from Theory and Experiment. *The Journal of Physical Chemistry Letters*, **7**, 2579-2585. https://doi.org/10.1021/acs.jpclett.6b01041

[9] Lei, H., Hardy, D. and Gao, F. (2021) Lead-Free Double Perovskite $Cs_2AgBiBr_6$: Fun-

damentals, Applications, and Perspectives. *Advanced Functional Materials*, **31**, Article 2105898. https://doi.org/10.1002/adfm.202105898

[10] Meyer, E.E., Egger, D.A., Kronik, L., *et al.* (2021) Lead-Free Halide Double Perovskites: Structural, Optical and Stability Properties. *Materials Today Physics*, **19**, Article 100403.

[11] Tress, W. and Sirtl, M.T. (2021) $Cs_2AgBiBr_6$ Double Perovskites as Lead-Free Alternatives for Perovskite Solar Cells? *Solar RRL*, **6**, Article 2100770. https://doi.org/10.1002/solr.202100770

[12] Ji, F., Klarbring, J., Wang, F., Ning, W., Wang, L., Yin, C., *et al.* (2020) Lead-Free Halide Double Perovskite $Cs_2AgBiBr_6$ with Decreased Band Gap. *Angewandte Chemie International Edition*, **59**, 15191-15194. https://doi.org/10.1002/anie.202005568

[13] Wright, A.D., Buizza, L.R.V., Savill, K.J., Longo, G., Snaith, H.J., Johnston, M.B., *et al.* (2021) Ultrafast Excited-State Localization in $Cs_2AgBiBr_6$ Double Perovskite. *The Journal of Physical Chemistry Letters*, **12**, 3352-3360. https://doi.org/10.1021/acs.jpclett.1c00653

[14] Rahman, N., Husain, M., Azzouz-Rached, A., Al-Ammar, E.A., Sfina, N., Alawaideh, Y.M., *et al.* (2024) Theoretical Investigations of Double Perovskites Rb_2YCuX_6 (X = Cl, F) for Green Energy Applications: DFT Study. *Journal of Physics and Chemistry of Solids*, **193**, Article 112171. https://doi.org/10.1016/j.jpcs.2024.112171

[15] Shah, S.A., Khan, S., Ali, A., *et al.* (2024) Exploring Rb_2YCuCl_6 and Cs_2YCuCl_6 Double Perovskites. *ACS Omega*, **9**, Article 22345.

[16] Hohenberg, P. and Kohn, W. (1964) Inhomogeneous Electron Gas. *Physical Review*, **136**, B864-B871. https://doi.org/10.1103/physrev.136.b864

[17] Kohn, W. and Sham, L.J. (1965) Self-Consistent Equations Including Exchange and Correlation Effects. *Physical Review*, **140**, A1133-A1138. https://doi.org/10.1103/physrev.140.a1133

[18] Perdew, J.P., Burke, K. and Ernzerhof, M. (1996) Generalized Gradient Approximation Made Simple. *Physical Review Letters*, **77**, 3865-3868. https://doi.org/10.1103/physrevlett.77.3865

[19] Payne, M.C., Teter, M.P., Allan, D.C., Arias, T.A. and Joannopoulos, J.D. (1992) Iterative Minimization Techniques for *ab Initio* Total-Energy Calculations: Molecular Dynamics and Conjugate Gradients. *Reviews of Modern Physics*, **64**, 1045-1097. https://doi.org/10.1103/revmodphys.64.1045

[20] Giannozzi, P., Baroni, S., Bonini, N., Calandra, M., Car, R., Cavazzoni, C., *et al.* (2009) QUANTUM ESPRESSO: A Modular and Open-Source Software Project for Quantum Simulations of Materials. *Journal of Physics: Condensed Matter*, **21**, Article 395502. https://doi.org/10.1088/0953-8984/21/39/395502

[21] Giannozzi, P., Andreussi, O., Brumme, T., Bunau, O., Buongiorno Nardelli, M., Calandra, M., *et al.* (2017) Advanced Capabilities for Materials Modelling with Quantum Espresso. *Journal of Physics: Condensed Matter*, **29**, Article 465901. https://doi.org/10.1088/1361-648x/aa8f79

[22] Giannozzi, P., Baseggio, O., Bonfà, P., Brunato, D., Car, R., Carnimeo, I., *et al.* (2020) Quantum ESPRESSO toward the Exascale. *The Journal of Chemical Physics*, **152**, Article 154105. https://doi.org/10.1063/5.0005082

[23] Monkhorst, H.J. and Pack, J.D. (1976) Special Points for Brillouin-Zone Integrations. *Physical Review B*, **13**, 5188-5192. https://doi.org/10.1103/physrevb.13.5188

[24] Vanderbilt, D. (1990) Soft Self-Consistent Pseudopotentials in a Generalized Eigenvalue Formalism. *Physical Review B*, **41**, 7892-7895.

https://doi.org/10.1103/physrevb.41.7892

[25] Hamann, D.R. (2013) Optimized Norm-Conserving Vanderbilt Pseudopotentials. *Physical Review B*, **88**, Article 085117. https://doi.org/10.1103/physrevb.88.085117

[26] Blöchl, P.E., Jepsen, O. and Andersen, O.K. (1994) Improved Tetrahedron Method for Brillouin-Zone Integrations. *Physical Review B*, **49**, 16223-16233. https://doi.org/10.1103/physrevb.49.16223

[27] Kresse, G. and Furthmüller, J. (1996) Efficient Iterative Schemes for *ab Initio* Total-Energy Calculations Using a Plane-Wave Basis Set. *Physical Review B*, **54**, 11169-11186. https://doi.org/10.1103/physrevb.54.11169

[28] Kresse, G. and Furthmüller, J. (1996) Efficiency of *Ab-Initio* Total Energy Calculations for Metals and Semiconductors Using a Plane-Wave Basis Set. *Computational Materials Science*, **6**, 15-50. https://doi.org/10.1016/0927-0256(96)00008-0

[29] Baroni, S., de Gironcoli, S., Dal Corso, A. and Giannozzi, P. (2001) Phonons and Related Crystal Properties from Density-Functional Perturbation Theory. *Reviews of Modern Physics*, **73**, 515-562. https://doi.org/10.1103/revmodphys.73.515

[30] Murnaghan, F.D. (1944) The Compressibility of Media under Extreme Pressures. *Proceedings of the National Academy of Sciences*, **30**, 244-247. https://doi.org/10.1073/pnas.30.9.244

[31] Birch, F. (1947) Finite Elastic Strain of Cubic Crystals. *Physical Review*, **71**, 809-824. https://doi.org/10.1103/physrev.71.809

[32] Bardeen, J. and Shockley, W. (1950) Deformation Potentials and Mobilities in Non-Polar Crystals. *Physical Review*, **80**, 72-80. https://doi.org/10.1103/physrev.80.72

[33] Ashcroft, N.W. and Mermin, N.D. (1976) Solid State Physics. Holt-Saunders.

[34] Kittel, C. (2005) Introduction to Solid State Physics. 8th Edition, Wiley.

[35] Ziman, J.M. (1972) Principles of the Theory of Solids. 2nd Edition, Cambridge University Press. https://doi.org/10.1017/cbo9781139644075

[36] Martin, R.M. (2004) Electronic Structure. Cambridge University Press. https://doi.org/10.1017/cbo9780511805769

[37] Sze, S.M. and Ng, K.K. (2006) Physics of Semiconductor Devices. Wiley. https://doi.org/10.1002/0470068329

[38] Tailor, N.K., Listorti, A., Colella, S. and Satapathi, S. (2023) Lead-Free Halide Double Perovskites: Fundamentals, Challenges, and Photovoltaics Applications. *Advanced Materials Technologies*, **8**, Article 2200942. https://doi.org/10.1002/admt.202200442